

VectorMapNet: End-to-end Vectorized HD Map Learning

Yicheng Liu¹ Yue Wang² Yilun Wang³ Hang Zhao^{1*}
¹Tsinghua University ²MIT ³Li Auto

Abstract: Autonomous driving systems require a good understanding of surrounding environments, including moving obstacles and static High-Definition (HD) semantic map elements. Existing methods approach the semantic map problem by offline manual annotation, which suffers from serious scalability issues. Recent learning-based methods produce dense rasterized segmentation predictions to construct maps. However, these predictions do not include instance information of individual map elements and require heuristic post-processing, that involves many hand-designed components, to obtain vectorized maps. To that end, we introduce an end-to-end vectorized HD map learning pipeline, termed VectorMapNet. VectorMapNet takes onboard sensor observations and predicts a sparse set of polylines primitives in the bird’s-eye view to model the geometry of HD maps. This pipeline can explicitly model the spatial relation between map elements and generate vectorized maps that are friendly to downstream autonomous driving tasks without the need for post-processing. In our experiments, VectorMapNet achieves strong HD map learning performance on nuScenes dataset, surpassing previous state-of-the-art methods by 14.2 mAP. Qualitatively, we also show that VectorMapNet is capable of generating comprehensive maps and capturing more fine-grained details of road geometry. To the best of our knowledge, VectorMapNet is the first work designed toward end-to-end vectorized HD map learning problems. Our project website is available at <https://tsinghua-mars-lab.github.io/vectormapnet/>.

Keywords: Autonomous Driving, Map Learning, Transformer

1 Introduction

Autonomous driving system requires an understanding of map elements on the road, including lanes, pedestrian crossing, and traffic signs, to navigate the world and to plan ahead. Such map elements are typically provided by pre-annotated High-Definition (HD) semantic maps in existing pipelines [1]. These methods suffer from serious scalability issues as human efforts are heavily involved in annotating HD maps. Recent works [2, 3, 4] explore the problem of online HD semantic map learning, where the goal is to use onboard sensors (*e.g.* LiDARs and cameras) to estimate map elements on-the-fly.

Most recent methods [4, 5, 3, 6] consider HD semantic map learning as a semantic segmentation problem in bird’s-eye view (BEV), which rasterizes map elements into pixels and assigns each pixel with a class label. This formulation makes it straightforward to leverage fully convolutional networks. However, rasterized maps are not an ideal map representation for autonomous driving for three reasons. First, rasterized maps lack instance information which is necessary to distinguish map elements with the same class label but different semantics, *e.g.* left turn lanes and right turn lanes. Second, it is hard to enforce consistency within the predicted rasterized maps, *e.g.* nearby lane pixels might have contradicted semantics or geometries. Third, rasterized maps are incompatible with most autonomous driving systems as these systems commonly employ instance-level vectorized representation for downstream tasks such as motion forecasting and planning. To alleviate these issues and produce vectorized outputs, HDMapNet [2] generates semantic, instance, and directional maps and vectorizes these three maps with a hand-designed post-processing algorithm.

*Correspond to hangzhao@mail.tsinghua.edu.cn

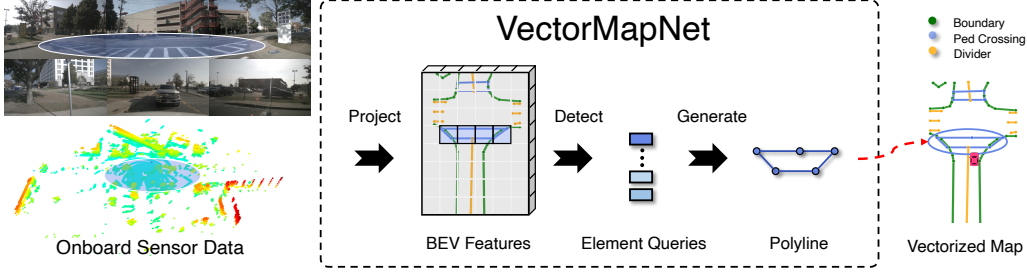


Figure 1: An overview of VectorMapNet. Sensor data is encoded to BEV features in the same coordinate as map elements. VectorMapNet detects the locations of map elements from BEV features by leveraging element queries. The vectorized HD map is built upon a sparse set of polylines that are generated from the detection results.

However, HDMapNet still relies on the rasterized map predictions, and its heuristic post-processing step complicates the pipeline and restricts the model’s scalability and performance. In this paper, we propose an end-to-end vectorized HD map learning model named VectorMapNet, which does not involve a dense set of semantic pixels. Instead, it represents map elements as a set of polylines that are closely related to downstream tasks, *e.g.* motion forecasting [7]. Therefore, the map learning problem boils down to predicting a sparse set of polylines from sensor observations in our paper. We leverage state-of-the-art set prediction and sequence generation methods to predict an HD map in the following steps. First, VectorMapNet aggregates features generated from different modalities (*e.g.* camera images and LiDAR) into a common BEV feature space. Then, it detects map elements’ locations based on learnable element queries and BEV features. Finally, we generate a polyline for each map element. An overview of VectorMapNet is shown in Figure 1.

Our experiments show that VectorMapNet achieves dominant performance on the public nuScenes dataset, outperforming HDMapNet and another baseline by at least 14.2 mAP. Qualitatively, We find that VectorMapNet builds a more comprehensive map compared to previous works and is capable of capturing fine details, *e.g.* jagged boundaries. Furthermore, we feed our predicted vectorized HD map into a downstream motion forecasting module, and show the compatibility and effectiveness of the predicted map.

To summarize, the contributions of the paper are as follows:

- VectorMapNet is an end-to-end HD semantic map learning method. Unlike previous works, it uses polylines to represent map elements and directly predicts vectorized outputs from sensor observations without requiring map rasterization or post-processing.
- Jointly modeling the topological relations between map elements and the geometry of each map element is challenging. We leverage polylines as primitives to model complex map elements and mitigate this difficulty by decoupling this joint module into two parts: a map element detector and a polyline generator.
- VectorMapNet achieves state-of-the-art HD semantic map learning performance on the nuScenes dataset. Qualitative results and downstream evaluations also validate our design choices.

2 VectorMapNet

Problem formulation. Similar to HDMapNet [2], our task is to model map elements in a vectorized form using data from onboard sensors, *e.g.* RGB cameras and/or LiDARs. These map elements include but are not limited to road boundaries, lane dividers, and pedestrian crossings, which are critical for autonomous driving.

We formulate this task as a sparse set prediction problem. Specifically, we represent a map \mathcal{M} by a sparse set of compact vectorized primitives, and the problem is to learn a model that extracts information from sensors to predict these primitives for representing the semantic map. We opt to use N polylines $\mathcal{V}^{\text{poly}} = \{V_1^{\text{poly}}, \dots, V_N^{\text{poly}}\}$ to represent these map elements. Each polyline $V_i^{\text{poly}} = \{v_{i,n} \in \mathbb{R}^2 | n = 1, \dots, N_v\}$ is a collection of N_v ordered vertices $v_{i,n}$.

Using polylines to represent map elements has three main advantages: (1) HD maps are typically composed of a mixture of different geometries, such as points, lines, curves, and polygons. Polylines

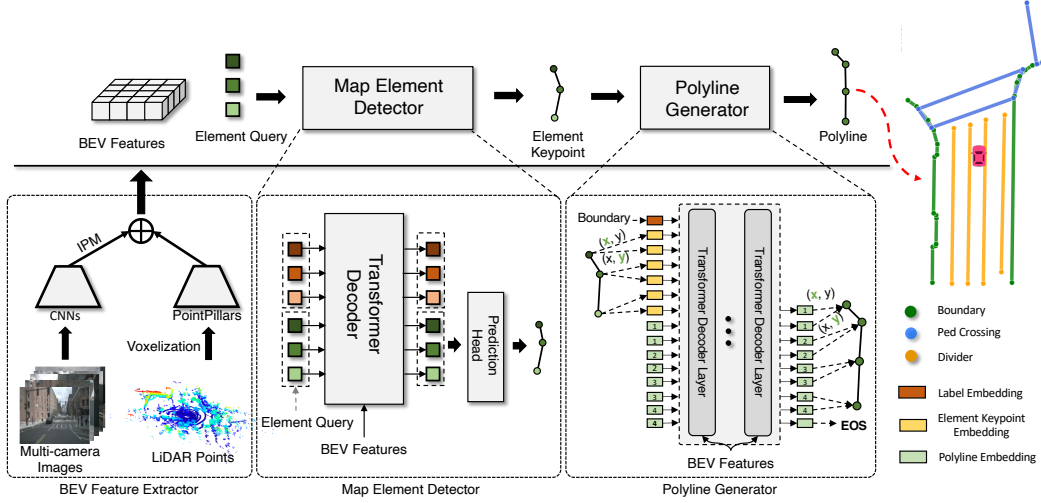


Figure 2: The network architecture of VectorMapNet. The top row is the pipeline of VectorMapNet generating polylines from raw sensor inputs. The bottom row illustrates detailed structures and inference procedures of three primary components of VectorMapNet: BEV feature extractor, map element detector, and polyline generator.

are a flexible primitive that can represent these geometric elements effectively. (2) The order of polyline vertices is a natural way to encode the direction of map elements, which is vital to driving. (3) The polyline representation has been widely used by downstream autonomous driving modules, such as motion forecasting [7].

Method overview. First, we map sensor data from sensor-view to a canonical BEV representation \mathcal{F}_{BEV} . Then the remaining task is to model polylines based on \mathcal{F}_{BEV} . However, map elements exhibit complicated and diverse structural and location patterns, learning both of them jointly can be challenging. Thus, we decouple the task into two parts: (1) A scene-level element detection task that locates and classifies all map elements by predicting element keypoints $\mathcal{A} = \{a_i \in \mathbb{R}^{k \times 2} | i = 1, \dots, N\}$ and their class labels $\mathcal{L} = \{l_i \in \mathbb{Z} | i = 1, \dots, N\}$; (2) An object-level sequence generation task that produces a sequence of polyline vertices for each detected map element (a_i, l_i) . The definition of element keypoint representation \mathcal{A} is described in § 2.2.

Correspondingly, VectorMapNet employs three modules to model these three tasks, as shown in Figure 2. (1) A BEV feature extractor that lifts sensor observations to BEV space (§ 2.1); (2) A map element detector that predicts map element keypoints \mathcal{A} and class labels \mathcal{L} (§ 2.2); (3) A polyline generator that completes the shapes of the HD map elements conditioned on keypoints and class labels (§ 2.3).

2.1 BEV Feature Extractor

The BEV feature extractor lifts various modality inputs into a unified feature space and aggregates these features into a canonical representation termed BEV features \mathcal{F}_{BEV} . We consider two common modalities: surrounding camera images \mathcal{I} and LiDAR points \mathcal{P} .

Camera branch. For image data \mathcal{I} , we use a shared CNN backbone to obtain each camera’s image features in the camera space, then use the Inverse Perspective Mapping (IPM) [8] technique to transform these features into BEV space. Since the depth information is missing in camera images, we follow one common approach that assumes the ground is mostly planar and transforms the images to BEV via homography. Without knowing the exact height of the ground plane, this homography is not an accurate transformation. To alleviate this issue, we transform the image features into four BEV planes with different heights (we use $(-1m, 0m, 1m, 2m)$ in practice). The camera BEV features $\mathcal{F}_{\text{BEV}}^{\mathcal{I}} \in \mathbb{R}^{W \times H \times C_1}$ are the concatenation of these feature maps.

LiDAR branch. For LiDAR data \mathcal{P} , we use a variant of PointPillars [9] with dynamic voxelization [10], which divides the 3D space into multiple pillars and uses pillar-wise point clouds to learn pillar-wise feature maps. We denote this feature map in BEV as $\mathcal{F}_{\text{BEV}}^{\mathcal{P}} \in \mathbb{R}^{W \times H \times C_2}$.

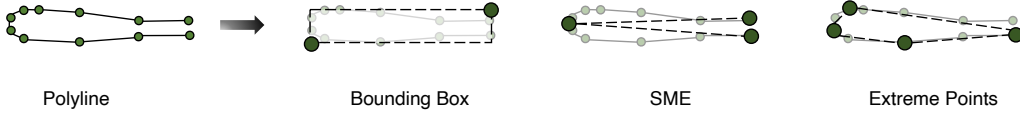


Figure 3: Keypoint representations of map elements. Three different keypoint representations are proposed here: Bounding Box ($k=2$), SME ($k=3$), and Extreme Points ($k=4$).

For sensor fusion, we obtain the BEV features $\mathcal{F}_{\text{BEV}} \in \mathbb{R}^{W \times H \times (C_1 + C_2)}$ by concatenating $\mathcal{F}_{\text{BEV}}^{\mathcal{T}}$ and $\mathcal{F}_{\text{BEV}}^{\mathcal{P}}$, and then process the concatenated result with a two-layer convolutional network. An overview of the BEV feature extractor is shown at the bottom-left of Figure 2. Since we use architectures similar to transformer in following modules, we flatten the BEV features \mathcal{F}_{BEV} into a sequence $\mathcal{F}_{\text{BEV}}^f \in \mathbb{R}^{WH \times (C_1 + C_2)}$. We also add fixed positional encodings to the sequence to retain spatial relations.

2.2 Map Element Detector

After obtaining BEV features, the goal of map element detector is to infer element keypoints $a_{i,j}$ from the BEV features \mathcal{F}_{BEV} . We leverage a variant of transformer set prediction detector [11] to achieve this goal. This detector represents map elements’ locations and categories by predicting their element keypoints \mathcal{A} and class labels \mathcal{L} . The geometric relations between these elements are modeled by the attention module in the detector. The detector is trained with bipartite matching loss, thus avoiding post-processing steps like non-maximum suppression (NMS).

Element queries. The query inputs of the detector are learnable element queries $\{q_i^{\text{elem}} \in \mathbb{R}^{k \times d} | i = 1, \dots, N_{\text{max}}\}$, where d is the hidden embedding size, and the i -th element query q_i^{elem} is composed of k keypoint embeddings: $q_i^{\text{elem}} = \{q_{i,j}^{\text{kp}} \in \mathbb{R}^d | j = 1, \dots, k\}$.

Architecture. The overall architecture of our map element detector includes a transformer decoder [12] and a prediction head, as shown at the bottom-middle of Figure 2. The decoder transforms the element queries using multi-head self-/cross-attention mechanisms. In particular, we use the deformable attention module [13] as the decoder’s cross attention module, where each element query has a 2D location grounding. It improves interpretability and accelerates training convergence [14].

The prediction head has two MLPs, which decodes element queries into element keypoints $a_{i,j} = \text{MLP}_{\text{kp}}(q_{i,j}^{\text{kp}})$ and their class labels $l_i = \text{MLP}_{\text{cls}}([q_{i,1}^{\text{kp}}, \dots, q_{i,k}^{\text{kp}}])$, respectively. $[\cdot]$ is a concatenation operator.

Keypoint representation of map elements. We use keypoints to represent the location and outline of map elements in a compact way. Since there is no straightforward keypoint design for polylines, we propose three simple representations as shown in Figure 3: *Bounding Box (Bbox)*, which is the smallest box enclosing a polyline, and its keypoints are defined as the top-right and bottom-left points of the box; *Start-Middle-End (SME)*, which consists of the start, middle, and end point of a polyline; *Extreme Points*, which are the left-most, right-most, top-most, and bottom-most points of a polyline. We conduct a further ablation study to evaluate their performance in § 3.3. Since Bbox performs the best in ablations, without further specification, all experiments used Bbox as the default keypoint representation.

Keypoint embeddings. Each keypoint embedding $q_{i,j}^{\text{kp}}$ in the map element detector has two learnable embeddings for the attention modules to identify the difference between keypoints. The first embedding is keypoint position embedding $\{e_j^{\text{kp}} \in \mathbb{R}^d | j = 1, \dots, k\}$, indicating which position the point belongs to in an element keypoint. The second embedding $\{e_i^{\text{p}} \in \mathbb{R}^d | i = 1, \dots, N_{\text{max}}\}$ encodes which map element the keypoint belongs to. The keypoint embedding $q_{i,j}^{\text{kp}}$ is the addition of these two embeddings $e_i^{\text{p}} + e_j^{\text{kp}}$.

Table 1: Comparison with baseline methods. Fusion denotes the model using both images and LiDAR points as inputs.

Methods	AP _{ped}	AP _{divider}	AP _{boundary}	mAP
STSU[17]	7.0	11.6	16.5	11.7
HDMaNet (Camera) [2]	14.4	21.7	33.0	23.0
HDMaNet (LiDAR) [2]	10.4	24.1	37.9	24.1
HDMaNet (Fusion) [2]	16.3	29.6	46.7	31.0
VectorMapNet (Camera)	36.1	47.3	39.3	40.9
VectorMapNet (LiDAR)	25.7	37.6	38.6	34.0
VectorMapNet (Fusion)	37.6	50.5	47.5	45.2

2.3 Polyline Generator

Given the label and keypoints of map elements, the goal of polyline generator is to generate detailed map element geometries (*i.e.*, polylines) from them. Specifically, polyline generator models a distribution $p(V_i^{\text{poly}}|a_i, l_i, \mathcal{F}_{\text{BEV}}^f)$ over the vertices of each polyline, conditioned on the initial layout (*i.e.*, element keypoints and class labels) and BEV features. To estimate this distribution, we decompose the joint distribution over V_i^{poly} as a product of a series of conditional vertex coordinate distributions. Specifically, we transform each polyline $V_i^{\text{poly}} = \{v_{i,n} \in \mathbb{R}^2 | n = 1, \dots, N_v\}$ into a flattened sequence $\{v_{i,n}^f \in \mathbb{R} | n = 1, \dots, 2N_v\}$ by concatenating coordinates values of polyline vertices and add an additional *End of Sequence* token (*EOS*) at the end of each sequence, and the target distribution turns into:

$$p(V_i^{\text{poly}}|a_i, l_i, \mathcal{F}_{\text{BEV}}^f; \theta) = \prod_{n=1}^{2N_v} p(v_{i,n}^f | v_{i,<n}^f, a_i, l_i, \mathcal{F}_{\text{BEV}}^f; \theta). \quad (1)$$

We model this distribution using an autoregressive network that outputs the parameters of a predictive distribution at each step for the next vertex coordinate. This predictive distribution is defined over all possible vertex coordinate values and *EOS*. Polyline generator is trained to maximize the log-probability of the observed polylines with respect to the model parameters θ and $\mathcal{F}_{\text{BEV}}^f$.

Vertices as discrete variables. Using discrete distributions to model polyline vertices has the advantage of representing arbitrary shapes, *i.e.*, categorical distributions can easily represent various polylines, such as multi-modal, skewed, peaked, or long-tailed, that are commonly seen in our task. Thus, we quantize the coordinate values into discrete tokens and model each token with a categorical distribution. We also conduct an ablation study in § 3.3 to investigate other modeling choices.

Architecture. The autoregressive network we choose is a vanilla transformer [12] (see the bottom-right of Figure 2). Each polyline’s keypoint coordinates and class label are tokenized and fed in as the query inputs of the transformer decoder. Then a sequence of vertex tokens are fed into the transformer iteratively, integrating BEV features with cross-attention, and decoded as polyline vertices. Note that the generator can generate all polylines in parallel.

Vertex embeddings. Following PolyGen [15], we use an addition of three learned embeddings as the embedding of each vertex token: *Coordinate Embedding*, indicating whether the token represents *x* or *y* coordinate; *Position Embedding*, representing which vertex the token belongs to; *Value Embedding*, expressing the token’s quantized coordinate value.

3 Experiments

We experiment on the nuScenes [16] dataset and use average precision as the evaluation metric. The details of dataset settings (§ A.1), model (§ A.2), and metrics (§ A.3) are presented in the Appendix.

3.1 Comparison with baselines

We choose two closely related models as our baselines, HDMaNet [2] and STSU [17]. For HDMaNet, we directly take its vectorized results. STSU uses a transformer module to detect the moving objects and centerline segments. It uses an association head to piece the segments together as the

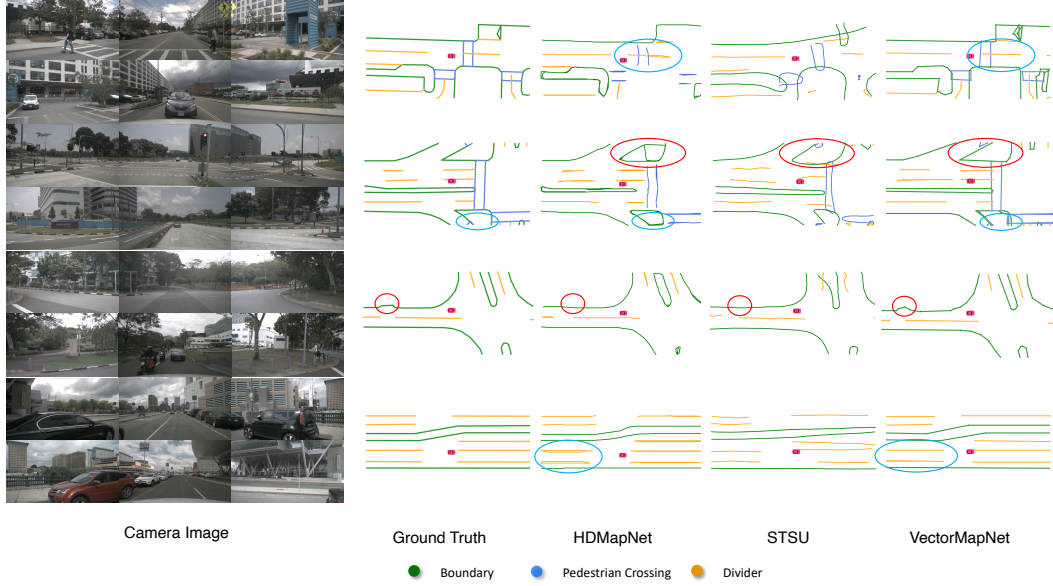


Figure 4: Qualitative results generated by VectorMapNet and baselines. We use camera images as inputs for comparisons. The areas enclosed by red and blue ellipses show that VectorMapNet can preserve sharp corners, and polyline representations prevent VectorMapNet from generating ambiguous self-looping results.

road graph. In order to adapt STSU to our task, we use a two-layer MLP to predict lane segments and only keep its object branch and polyline branch. We report the average precision that uses Chamfer distance as the threshold to determine the positive matches with ground truth. $\{0.5, 1.0, 1.5\}$ are the predefined thresholds of Chamfer distance AP.

As shown in Table 1, VectorMapNet outperforms HDMaPNet by a large margin under all settings (+17.9 mAP in Camera, +9.9 mAP in LiDAR, and +11.7 mAP in Fusion). Compared to camera-only and LiDAR-only, sensor fusion introduces +4.3 mAP improvement and +11.2 mAP improvement, respectively. STSU is -29.2 mAP lower than VectorMapNet. Since STSU treats all map elements as a set of fixed-size segments, we hypothesize that ignoring the geometry of map elements hurts the performance significantly.

3.2 Qualitative Analysis

Benefits of using polylines as primitives. From visualizations, we find that using polylines as primitives has brought us two benefits compared with baselines: First, polylines effectively encode the detailed geometries of map elements, *e.g.* the corners of boundaries (see the red ellipses in Figure 4). Second, polyline representations prevent VectorMapNet from generating ambiguous results, as it consistently encodes direction information. In contrast, Rasterized methods are prone to falsely generating loopy curves (see the blue ellipses in Figure 4). These ambiguities hinder safe autonomous driving. Therefore, the polyline is a desired primitive for map learning, as it can reflect real-world road layouts and explicitly encode directions.

Benefits of top-down modeling. VectorMapNet works in a top-down manner: it models the topology of the map and the map element locations first, and then generates map element details. Visualizations show that VectorMapNet capture the map elements comprehensively, including the small elements close to edges. The high mAP of VectorMapNet over other baselines further confirms this observation. Surprisingly, Figure 5 shows that VectorMapNet can find the map elements that are not annotated in the HD map provided by the dataset.

3.3 Ablation Studies

In this section, we explore how the sampling strategies of polyline vertices, modeling of polylines, and keypoint representations influence model performance. We report two types of average precisions:

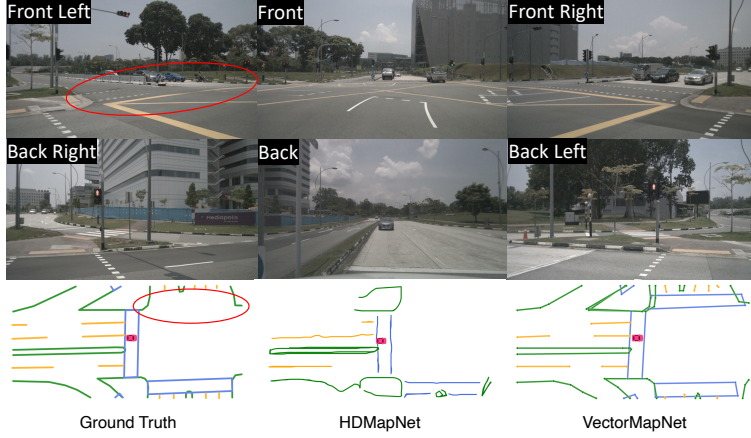


Figure 5: An example of VectorMapNet detecting unlabeled map elements. The red ellipse indicates a pedestrian crossing that is missing in ground truth annotations, while VectorMapNet detects it correctly. All the predictions are generated from camera images.

Chamfer AP and Fréchet AP (see definitions in § A.3). The threshold of Fréchet APs is chosen as $5m$, and the settings of Chamfer AP are the same as in § 3.1.

Table 2: Ablation study of curves sampling strategies.

Vertex Sampling Method	Fréchet Distance				Chamfer Distance			
	AP_{ped}	$AP_{divider}$	$AP_{boundary}$	mAP	AP_{ped}	$AP_{divider}$	$AP_{boundary}$	mAP
curvature-based	47.0	47.4	56.9	50.4	27.6	34.4	35.4	32.5
fixed interval	26.0	23.6	37.1	28.9	14.6	17.6	18.7	17.0

Curve sampling strategies. We use two approaches to sample polylines. The first is based on the original nuScenes setting [16], which samples vertices at the position where the curvature changes are beyond a certain threshold. The second is to sample the vertices at fixed intervals ($1m$). We compare our methods under these two sampling strategies and the results are shown in Table 2. The curvature-based sampling outperforms its fixed-sampling counterpart by a large margin and achieves a leading 21.5 Fréchet mAP and 15.5 Chamfer mAP. We hypothesize that the fixed-sampling method involves a large set of redundant vertices that have negligible contributions to the geometry, thus under-weighs the essential vertices (*e.g.* the vertices at the corner of a polyline) in the learning process.

Table 3: Ablation study of vertex modeling methods.

Modeling Method	Fréchet Distance				Chamfer Distance			
	AP_{ped}	$AP_{divider}$	$AP_{boundary}$	mAP	AP_{ped}	$AP_{divider}$	$AP_{boundary}$	mAP
discrete	47.0	47.4	56.9	50.4	27.6	34.4	35.4	32.5
continuous	38.0	41.6	46.1	41.9	26.5	28.1	30.1	26.5

Vertex modeling methods. We investigate both discrete and continuous ways to model polyline vertices. The discrete version of polyline generator is described in § 2.3. With the same model structure, we follow SketchRNN [18] and use mixture of Gaussian distributions to model the vertices of polylines as continuous variables. The comparison is shown in Table 3. We find that using discrete embeddings vertex coordinates results in a considerable gain in performance, with Chamfer mAP increasing from 18.2 to 32.5 and the Fréchet mAP increasing from 26.8 to 50.4. These improvements suggest that the non-local characteristic of categorical distribution helps our model to capture complex vertex coordinate distributions.

Keypoint representations. In the Method section, we propose three keypoint representations: bounding box (Bbox), Start-Middle-End (SME), and extreme points (Extreme). We remove the IoU loss when training the model with SME representations, as SME does not have a definition of areas (see loss details in § A.2). We experiment with these representations and list the results in Table 4. Our results show that the bounding box representation leads to the best mean average performance

Table 4: Ablation study of keypoint representaions.

Keypoint Representaion	k	Fréchet Distance				Chamfer Distance			
		AP_{ped}	$AP_{divider}$	$AP_{boundary}$	mAP	AP_{ped}	$AP_{divider}$	$AP_{boundary}$	mAP
Bbox	2	47.4	46.9	62.8	52.4	36.1	47.3	39.3	40.9
SME	3	47.0	47.4	56.9	50.4	27.6	34.4	35.4	32.5
Extreme	4	41.7	47.3	59.0	49.4	30.4	33.1	37.3	33.6

Table 5: Predicted map for motion forecasting. There are three input settings: past trajectories (denoted as Traj.), past trajectories with the human-annotated HD map from the nuScenes (denoted as Traj. + G.T. Map), and past trajectories with the predicted map from VectorMapNet (denoted as Traj. + Pred. Map). The predicted map greatly improves the prediction performance compared with the model that only use past trajectories.

Prediction Model Inputs	minADE ↓	minFDE ↓	MR@2m ↓
Traj.	0.909	1.577	19.6
Traj. + G.T. Map	0.779	1.390	18.0
Traj. + Pred. Map	0.826	1.477	18.2

in both metrics, outperforming others by 2.0 Fréchet mAP and 7.3 Chamfer mAP. SME seems to be the most suitable keypoint representation as it is naturally linked to polylines. Surprisingly, the performance of SME falls behind the Bbox by 5.0 Chamfer mAP. We hypothesize that the IoU loss [19] greatly improves the detector’s performance, similar to the observations reported by DETR [11], as optimizing the displacement of points with the smoothed L1 loss alone may not align well with the task performance.

3.4 Vectorized HD Map for Motion Forecasting

Since predicting future motions in the complex environment heavily relies on the map information, we investigate the effectiveness of our predicted HD map in this downstream motion forecasting task.

Task Settings. In our setting, the motion forecasting model aims to predict a target agent’s 6 plausible future trajectories (3 seconds) from past trajectories (1 second) of agents and an HD semantic map which covers an area of $60m \times 30m$. We generate data by sampling from nuScenes tracking dataset. We first retrieve agents observed in the tracking dataset and then select agents with complete 3-second future observations as the target agents. As a result, the dataset consists of 25,645 training samples and 5,460 test samples. We use three different input settings to investigate the performance of our predicted HD map: past trajectories, past trajectories with the ground truth HD map, and past trajectories with the map predicted by VectorMapNet. The motion forecaster we used is mmTransformer [20] which can optionally take vectorized maps and trajectories as inputs.

Results. To evaluate the performance of motion forecasting under different input settings, we report results on three commonly used metrics [21]: minimum average displacement error (minADE), minimum final displacement error (minFDE) and miss rate (MR). To get the results, these metrics only account for the best trajectory out of 6 predicted trajectories. Results in Table 5 show that the map predicted by VectorMapNet has encoded environment information that greatly helps the motion forecaster, compared with the model that only takes past trajectories as inputs. The gap between the ground-truth map and the predicted map is not big either, especially in terms of MR (-0.2%). We think future research could further close the performance gap.

4 Related Works

Semantic map learning. Annotating semantic maps attracts plenty of interests thanks to autonomous driving. Recently, semantic map learning is formulated as a semantic segmentation problem [22] and is solved by using aerial images [23], LiDAR points [5], and HD panorama [24]. The crowdsourcing tags [25] are used to improve the performance of fine-grained segmentation. Instead of using offline data, recent works focus on understanding BEV semantics from onboard camera images [26, 27], and videos [28]. Only using onboard sensors as model input is particularly challenging as the

inputs and target map lie in different coordinate systems. Recently, several cross-view learning approaches [3, 29, 2, 6?, 30] leverage the geometric structure of scenes to mitigate the mismatch between sensor inputs and BEV representations. Beyond pixel-level semantic maps, our work extracts a consistent vectorized map around vehicles from surrounding cameras or LiDARs, which suits for downstream tasks like motion forecasting [7, 31, 20].

Lane detection. Lane detection aims to separate lane segments from road scenes precisely. Most lane detection algorithms [32, 33] use a pixel-level segmentation technique combined with sophisticated post-processing. Another line of work leverages the predefined proposal to achieve high accuracy and fast inference speed. These methods typically involve handcrafted elements such as vanishing points [34], polynomial curves [35], line segments [36], and Bézier curves [37] to model proposals. In addition to using perspective view cameras as inputs, the authors of [38] and [39] extract lane segments from overhead highway cameras and LiDAR imagery with a recurrent neural network. Instead of discovering the road’s topology via boundaries detection, STSU [17] constructs lane graphs by using the centerline segment encoded by Bézier curve as primitive. To model complex geometries in the urban environment, we leverage polylines to represent the whole map elements in perceptual scope instead of handcrafted elements. Using polylines as primitive allows our method to model maps without complicated geometric assumptions and express map elements with arbitrary shapes.

Geometric data modeling. Another line of work closely related to VectorMapNet is geometric data generation. These methods typically treat geometric elements as a sequence, such as primitive parts of furniture [40, 41], states of sketch strokes [18], and vertices of n -gon mesh [15], and generate these sequences by leveraging autoregressive models. Since the directly modeling sequence is challenging for long-range centerline maps, HDMapGen [42] views the map as a two-level hierarchy. It produces a global and local graph separately with a hierarchical graph RNN. Instead of treating geometric elements as a sequence generation problem, LETR [43] models line segment as a detection problem and tackle it with a query-based detector. Unlike the above approaches that focus on single-level geometric modelings, such as scene level (*e.g.* line segments in an image) or object-level (*e.g.* furniture), VectorMapNet is designed to address both the scene level and object level geometric modeling. Specifically, VectorMapNet constructs a map by modeling the global relationship between map elements in the scene and the local geometric details inside each element.

5 Conclusions

We present VectorMapNet, an end-to-end model to tackle the HD semantic map learning problem. Unlike existing works, VectorMapNet uses polylines as the primitives to represent vectorized HD map elements. To learn these polylines, we decompose the learning problem into a detection and a generation problem. Our experiments show that VectorMapNet can generate coherent and complex geometries for urban map elements, benefiting from the polyline primitives. We believe that this novel way to learn HD maps provides a new perspective on the HD semantic map learning problem.

Limitations. Although our method can generate coherent and complex geometries in a single frame, temporally consistent predictions are not guaranteed. How to effectively encode temporal information for vectorized HD map prediction is challenging, which we leave as future work.

Acknowledgments

We would like to thank Qi Li, Tianyuan Zhang, and Tianyuan Yuan for their help on various baselines. We also thank Ziyuan Huang and Bowen Li for proofreading this paper draft.

References

- [1] G. Rong, B. H. Shin, H. Tabatabaee, Q. Lu, S. Lemke, M. Možeiko, E. Boise, G. Uhm, M. Gerow, S. Mehta, et al. Lgsvl simulator: A high fidelity simulator for autonomous driving. *arXiv preprint arXiv:2005.03778*, 2020.
- [2] Q. Li, Y. Wang, Y. Wang, and H. Zhao. Hdmapnet: A local semantic map learning and evaluation framework. *arXiv preprint arXiv:2107.06307*, 2021.

- [3] J. Phillion and S. Fidler. Lift, splat, shoot: Encoding images from arbitrary camera rigs by implicitly unprojecting to 3d. In *European Conference on Computer Vision*, pages 194–210. Springer, 2020.
- [4] T. Roddick and R. Cipolla. Predicting semantic map representations from images using pyramid occupancy networks. In *Proceedings of the IEEE/CVF Conference on Computer Vision and Pattern Recognition*, pages 11138–11147, 2020.
- [5] B. Yang, M. Liang, and R. Urtasun. Hdnet: Exploiting hd maps for 3d object detection. In *Conference on Robot Learning*, pages 146–155. PMLR, 2018.
- [6] B. Zhou and P. Krähenbühl. Cross-view transformers for real-time map-view semantic segmentation. *arXiv preprint arXiv:2205.02833*, 2022.
- [7] J. Gao, C. Sun, H. Zhao, Y. Shen, D. Anguelov, C. Li, and C. Schmid. Vectornet: Encoding hd maps and agent dynamics from vectorized representation. In *Proceedings of the IEEE/CVF Conference on Computer Vision and Pattern Recognition*, pages 11525–11533, 2020.
- [8] H. A. Mallot, H. H. Bülthoff, J. Little, and S. Bohrer. Inverse perspective mapping simplifies optical flow computation and obstacle detection. *Biological cybernetics*, 64(3):177–185, 1991.
- [9] A. H. Lang, S. Vora, H. Caesar, L. Zhou, J. Yang, and O. Beijbom. Pointpillars: Fast encoders for object detection from point clouds. In *Proceedings of the IEEE/CVF Conference on Computer Vision and Pattern Recognition*, pages 12697–12705, 2019.
- [10] Y. Zhou, P. Sun, Y. Zhang, D. Anguelov, J. Gao, T. Ouyang, J. Guo, J. Ngiam, and V. Vasudevan. End-to-end multi-view fusion for 3d object detection in lidar point clouds. In *Conference on Robot Learning*, pages 923–932. PMLR, 2020.
- [11] N. Carion, F. Massa, G. Synnaeve, N. Usunier, A. Kirillov, and S. Zagoruyko. End-to-end object detection with transformers. In *European conference on computer vision*, pages 213–229. Springer, 2020.
- [12] A. Vaswani, N. Shazeer, N. Parmar, J. Uszkoreit, L. Jones, A. N. Gomez, Ł. Kaiser, and I. Polosukhin. Attention is all you need. *Advances in neural information processing systems*, 30, 2017.
- [13] X. Zhu, W. Su, L. Lu, B. Li, X. Wang, and J. Dai. Deformable detr: Deformable transformers for end-to-end object detection. *arXiv preprint arXiv:2010.04159*, 2020.
- [14] F. Li, H. Zhang, S. Liu, J. Guo, L. M. Ni, and L. Zhang. Dn-detr: Accelerate detr training by introducing query denoising. *arXiv preprint arXiv:2203.01305*, 2022.
- [15] C. Nash, Y. Ganin, S. A. Eslami, and P. Battaglia. Polygen: An autoregressive generative model of 3d meshes. In *International Conference on Machine Learning*, pages 7220–7229. PMLR, 2020.
- [16] H. Caesar, V. Bankiti, A. H. Lang, S. Vora, V. E. Liong, Q. Xu, A. Krishnan, Y. Pan, G. Baldan, and O. Beijbom. nuscenes: A multimodal dataset for autonomous driving. In *Proceedings of the IEEE/CVF conference on computer vision and pattern recognition*, pages 11621–11631, 2020.
- [17] Y. B. Can, A. Liniger, D. P. Paudel, and L. Van Gool. Structured bird’s-eye-view traffic scene understanding from onboard images. In *Proceedings of the IEEE/CVF International Conference on Computer Vision*, pages 15661–15670, 2021.
- [18] D. Ha and D. Eck. A neural representation of sketch drawings. *arXiv preprint arXiv:1704.03477*, 2017.
- [19] H. Rezatofighi, N. Tsoi, J. Gwak, A. Sadeghian, I. Reid, and S. Savarese. Generalized intersection over union: A metric and a loss for bounding box regression. In *Proceedings of the IEEE/CVF conference on computer vision and pattern recognition*, pages 658–666, 2019.
- [20] Y. Liu, J. Zhang, L. Fang, Q. Jiang, and B. Zhou. Multimodal motion prediction with stacked transformers. In *Proceedings of the IEEE/CVF Conference on Computer Vision and Pattern Recognition*, pages 7577–7586, 2021.

- [21] M.-F. Chang, J. Lambert, P. Sangkloy, J. Singh, S. Bak, A. Hartnett, D. Wang, P. Carr, S. Lucey, D. Ramanan, et al. Argoverse: 3d tracking and forecasting with rich maps. In *Proceedings of the IEEE/CVF Conference on Computer Vision and Pattern Recognition*, pages 8748–8757, 2019.
- [22] G. Máttyus, S. Wang, S. Fidler, and R. Urtasun. Enhancing road maps by parsing aerial images around the world. In *Proceedings of the IEEE international conference on computer vision*, pages 1689–1697, 2015.
- [23] G. Máttyus, S. Wang, S. Fidler, and R. Urtasun. Hd maps: Fine-grained road segmentation by parsing ground and aerial images. In *Proceedings of the IEEE Conference on Computer Vision and Pattern Recognition*, pages 3611–3619, 2016.
- [24] S. Wang, M. Bai, G. Máttyus, H. Chu, W. Luo, B. Yang, J. Liang, J. Chéverie, S. Fidler, and R. Urtasun. Torontocity: Seeing the world with a million eyes. *arXiv preprint arXiv:1612.00423*, 2016.
- [25] S. Wang, S. Fidler, and R. Urtasun. Holistic 3d scene understanding from a single geo-tagged image. In *Proceedings of the IEEE Conference on Computer Vision and Pattern Recognition*, pages 3964–3972, 2015.
- [26] C. Lu, M. J. G. van de Molengraft, and G. Dubbelman. Monocular semantic occupancy grid mapping with convolutional variational encoder–decoder networks. *IEEE Robotics and Automation Letters*, 4(2):445–452, 2019.
- [27] W. Yang, Q. Li, W. Liu, Y. Yu, Y. Ma, S. He, and J. Pan. Projecting your view attentively: Monocular road scene layout estimation via cross-view transformation. In *Proceedings of the IEEE/CVF Conference on Computer Vision and Pattern Recognition*, pages 15536–15545, 2021.
- [28] Y. B. Can, A. Liniger, O. Unal, D. Paudel, and L. Van Gool. Understanding bird’s-eye view semantic hd-maps using an onboard monocular camera. *arXiv preprint arXiv:2012.03040*, 2020.
- [29] B. Pan, J. Sun, H. Y. T. Leung, A. Andonian, and B. Zhou. Cross-view semantic segmentation for sensing surroundings. *IEEE Robotics and Automation Letters*, 5(3):4867–4873, 2020.
- [30] X. Chen, T. Zhang, Y. Wang, Y. Wang, and H. Zhao. Futr3d: A unified sensor fusion framework for 3d detection. *arXiv preprint arXiv:2203.10642*, 2022.
- [31] H. Zhao, J. Gao, T. Lan, C. Sun, B. Sapp, B. Varadarajan, Y. Shen, Y. Shen, Y. Chai, C. Schmid, et al. Tnt: Target-driven trajectory prediction. *arXiv preprint arXiv:2008.08294*, 2020.
- [32] X. Pan, J. Shi, P. Luo, X. Wang, and X. Tang. Spatial as deep: Spatial cnn for traffic scene understanding. In *Proceedings of the AAAI Conference on Artificial Intelligence*, volume 32, 2018.
- [33] D. Neven, B. De Brabandere, S. Georgoulis, M. Proesmans, and L. Van Gool. Towards end-to-end lane detection: an instance segmentation approach. In *2018 IEEE intelligent vehicles symposium (IV)*, pages 286–291. IEEE, 2018.
- [34] S. Lee, J. Kim, J. Shin Yoon, S. Shin, O. Bailo, N. Kim, T.-H. Lee, H. Seok Hong, S.-H. Han, and I. So Kweon. Vpgnet: Vanishing point guided network for lane and road marking detection and recognition. In *Proceedings of the IEEE international conference on computer vision*, pages 1947–1955, 2017.
- [35] W. Van Gansbeke, B. De Brabandere, D. Neven, M. Proesmans, and L. Van Gool. End-to-end lane detection through differentiable least-squares fitting. In *Proceedings of the IEEE/CVF International Conference on Computer Vision Workshops*, pages 0–0, 2019.
- [36] X. Li, J. Li, X. Hu, and J. Yang. Line-cnn: End-to-end traffic line detection with line proposal unit. *IEEE Transactions on Intelligent Transportation Systems*, 21(1):248–258, 2019.

- [37] Z. Feng, S. Guo, X. Tan, K. Xu, M. Wang, and L. Ma. Rethinking efficient lane detection via curve modeling. *arXiv preprint arXiv:2203.02431*, 2022.
- [38] N. Homayounfar, W.-C. Ma, S. K. Lakshmikanth, and R. Urtasun. Hierarchical recurrent attention networks for structured online maps. In *Proceedings of the IEEE Conference on Computer Vision and Pattern Recognition*, pages 3417–3426, 2018.
- [39] J. Liang, N. Homayounfar, W.-C. Ma, S. Wang, and R. Urtasun. Convolutional recurrent network for road boundary extraction. In *Proceedings of the IEEE/CVF Conference on Computer Vision and Pattern Recognition*, pages 9512–9521, 2019.
- [40] J. Li, K. Xu, S. Chaudhuri, E. Yumer, H. Zhang, and L. Guibas. Grass: Generative recursive autoencoders for shape structures. *ACM Transactions on Graphics (TOG)*, 36(4):1–14, 2017.
- [41] K. Mo, P. Guerrero, L. Yi, H. Su, P. Wonka, N. Mitra, and L. J. Guibas. Structurenets: Hierarchical graph networks for 3d shape generation. *arXiv preprint arXiv:1908.00575*, 2019.
- [42] L. Mi, H. Zhao, C. Nash, X. Jin, J. Gao, C. Sun, C. Schmid, N. Shavit, Y. Chai, and D. Anguelov. Hdmapgen: A hierarchical graph generative model of high definition maps. In *Proceedings of the IEEE/CVF Conference on Computer Vision and Pattern Recognition*, pages 4227–4236, 2021.
- [43] Y. Xu, W. Xu, D. Cheung, and Z. Tu. Line segment detection using transformers without edges. In *Proceedings of the IEEE/CVF Conference on Computer Vision and Pattern Recognition*, pages 4257–4266, 2021.
- [44] K. He, X. Zhang, S. Ren, and J. Sun. Deep residual learning for image recognition. In *Proceedings of the IEEE conference on computer vision and pattern recognition*, pages 770–778, 2016.
- [45] C. R. Qi, H. Su, K. Mo, and L. J. Guibas. Pointnet: Deep learning on point sets for 3d classification and segmentation. In *Proceedings of the IEEE conference on computer vision and pattern recognition*, pages 652–660, 2017.
- [46] I. Loshchilov and F. Hutter. Fixing weight decay regularization in adam. 2018.
- [47] T. Eiter and H. Mannila. Computing discrete fréchet distance. 1994.
- [48] P. K. Agarwal, R. B. Avraham, H. Kaplan, and M. Sharir. Computing the discrete fréchet distance in subquadratic time. *SIAM Journal on Computing*, 43(2):429–449, 2014.

A Experiment Setup

A.1 Dataset

We experiment on nuScenes [16] dataset, which contains 1000 sequences of recordings collected by autonomous driving cars. Each episode is annotated at 2Hz and contains 6 camera images and LiDAR sweeps. Our dataset setup and pre-processing steps are identical to that of HDMapNet [2], which includes three categories of map elements – pedestrian crossing, divider, and road boundary – from the nuScenes dataset.

A.2 Implementation details

Architectures. BEV feature extractor outputs a feature map with a size of (200, 100, 128). It uses ResNet50 [44] for shared CNN backbone. We use a single layer PointNet [45] whose outputs have 64 dimensions as the LiDAR backbone to aggregate LiDAR points into a pillar. We set the number of element queries N_{\max} in map element detector as 100. The transformer decoders we used in map element detector and polyline generator both have 6 decoder layers, and their hidden embeddings’ size is 256. For the output space of polyline generator, we divide the map space (see § 2.3) evenly into 200×100 rectangular grids, and each grid has a size of $0.3m \times 0.3m$.

Training strategy. We train all our models on 8 GTX3090 GPUs for 110 epochs with a total batch size of 32. We use AdamW [46] optimizer with a gradient clipping norm of 5.0. For the learning

rate schedule, we use a step schedule that multiplies a learning rate by 0.1 at epoch 100 and has a linear warm-up period at the first 5000 steps. The dropout rate for all modules is 0.2, following the transformer’s settings [12]. Data augmentation is only deployed during polyline generator’s training; specifically, two I.I.D. Gaussian noises are added to each input vertex’s x and y coordinates with a probability of 0.3.

Loss functions. The loss function of map element detector is a linear combination of three parts: a negative log-likelihood for element keypoint classification, a smooth L1 loss, and an IoU loss for keypoints regression. The coefficients of these loss components are 2, 0.1, 1. The matching cost of map element detector is the same as the loss combination. The loss function of polyline generator is a negative log-likelihood. We train VectorMapNet by simply summing up these losses.

A.3 Metrics

In contrast to existing methods which generate rasterized results, our method does not require rasterizing curves on grids. Therefore, we opt not to use Intersection-Over-Union (IoU) as a metric. We use a distance-based metric to evaluate the similarity between predicted curves and ground-truth curves. We follow the instance-level evaluation metric proposed by HDMaNet [2] to compare the instance-level detection performance of our model to baseline methods. The metric is average precision (AP), where positive/negative samples are based on geometric similarity, more concretely, Chamfer distance and Fréchet distance. For clarity, we call the AP based on Chamfer distance and Fréchet distance as Chamfer AP and Fréchet AP, respectively.

Chamfer distance. Chamfer distance is a distance measure that quantifies the similarity between two *unordered* sets. The Chamfer distance is an evaluation metric that quantifies the similarity between two unordered sets by taking into account the distance of each permutation of the elements of set as follows:

$$D_{chamfer}(\mathcal{S}_1, \mathcal{S}_2) = \frac{1}{2} \left(\frac{1}{|\mathcal{S}_1|} \sum_{p \in \mathcal{S}_1} \min_{q \in \mathcal{S}_2} \|p, q\|_2 + \frac{1}{|\mathcal{S}_2|} \sum_{q \in \mathcal{S}_2} \min_{p \in \mathcal{S}_1} \|q, p\|_2 \right). \quad (2)$$

In our experiments, we use chamfer distance to calculate the distance between a prediction and a ground truth polyline set, and each polyline set is represented by uniformly sampling a polyline to N_{pts} vertices, where N_{pts} is set to 100 in our experiments.

Fréchet distance. The order of polyline vertices is not measured by Chamfer distance. Therefore, we introduce Fréchet distance as an additional measure. Fréchet distance is a measure of similarity of curves that takes both the positions and the *order* of the points along the curves into consideration. Our implementation is based on discrete Fréchet distance [47, 48].

We use the discrete version of Fréchet distance [47, 48] to evaluate the geometric similarity between two polyline P and Q . We denote $\sigma(P)$ as a sequence of endpoints of the line segments of P . In particular, $\sigma(P) = (p_1, \dots, p_m)$ is a sequence with m vertices that uniformly sampled from the original input polyline P , where each position of P between p_i and p_{i+1} can be approximated by using an affine transformation that is $p_{i+\lambda} = (1 - \lambda)p_i + \lambda p_{i+1}$ and the m in our experiment is set as 100.

Let P and Q be polyline and $\sigma(P) = (u_1, \dots, u_p)$ and $\sigma(Q) = (v_1, \dots, v_q)$ the corresponding sequences. A coupling L is a sequence of distinct pairs between $\sigma(P)$ and $\sigma(Q)$:

$$(u_{a_1}, v_{b_1}), \dots, (u_{a_m}, v_{b_m}). \quad (3)$$

These indexes $\{a_1, \dots, a_m\}$ and $\{b_1, \dots, b_m\}$ are nondecreasing surjection such that $a_1 = 1$, $a_m = p$, $b_1 = 1$, $b_m = q$ and for all $i < j \in \{1, \dots, m\}$, $a_i \leq a_j$ and $b_i \leq b_j$.

We define the norm $\|L\|$ of the L is the length of the longest pair in L , that is,

$$\|L\| = \max_{i=1, \dots, m} d(u_{a_i}, v_{b_i}). \quad (4)$$

The discrete Fréchet distance between polyline P and Q is defined to be

$$\delta_{dF}(P, Q) = \min\{\|L\|, L \text{ is a coupling between } P \text{ and } Q\}. \quad (5)$$

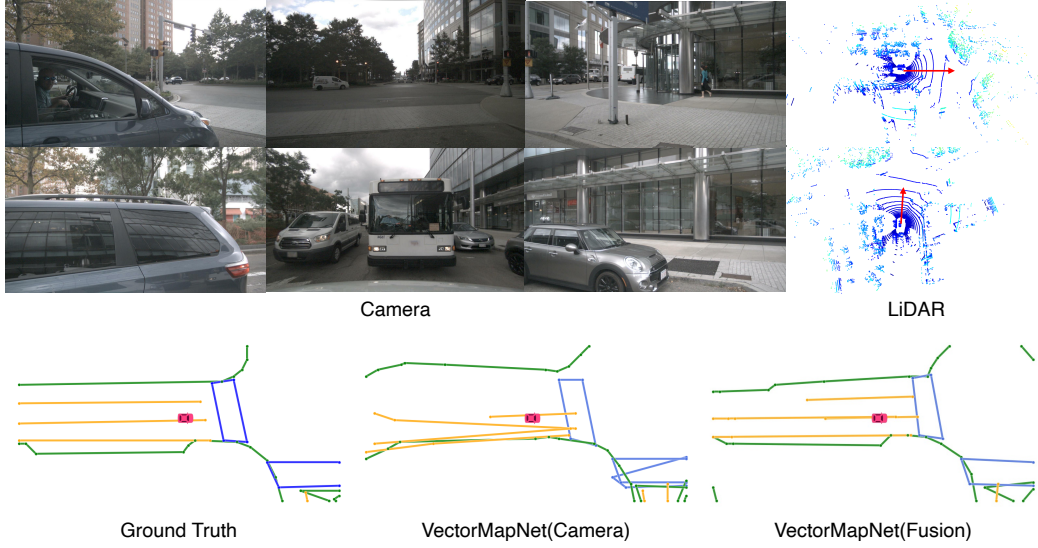


Figure 6: When the ego car cameras are occluded by the nearby vehicles, VectorMapNet(Camera) can not precept the surrounding map. With the depth cue from LiDAR, VectorMapNet(Fusion) can generate a more plausible result than its camera counterpart.

This equation indicates that the distance of discrete Fréchet distance is the minimum norm of all possible couplings. To Find the coupling plausible L that has the minimum norm, we use a Dynamic programming-based algorithm that is described in Algorithm 1.

Algorithm 1: The Algorithm of Discrete Fréchet Distance

Input: polyline $P = (u_1, \dots, u_p)$ and $Q = (v_1, \dots, v_q)$.

Output: $\delta_{dF}(P, Q)$

ca : an 2d array of real with size of $(p \times q)$;

Function $c(i, j)$

```

    if  $ca(i, j) > -1$  then
        return  $ca(i, j)$ ;
    else if  $i = 1$  and  $j = 1$  then
         $ca(i, j) := d(u_1, v_1)$ ;
    else if  $i > 1$  and  $j = 1$  then
         $ca(i, j) := \max\{c(i-1, 1), d(u_i, v_1)\}$ ;
    else if  $i = 1$  and  $j > 1$  then
         $ca(i, j) := \max\{c(1, j-1), d(u_1, v_j)\}$ ;
    else if  $i > 1$  and  $j > 1$  then
         $ca(i, j) := \max\{\min(c(i-1, j), c(i-1, j-1), c(i, j-1)), d(u_i, v_j)\}$ ;
    else
         $ca(i, j) := \infty$ ;
    end
    return  $ca(i, j)$ ;

```

end

begin

```

    for  $i = 1$  to  $p$  do
        for  $j = 1$  to  $q$  do
             $ca(i, j) := -1.0$ ;
        end
    end
    return  $c(p, q)$ ;

```

end

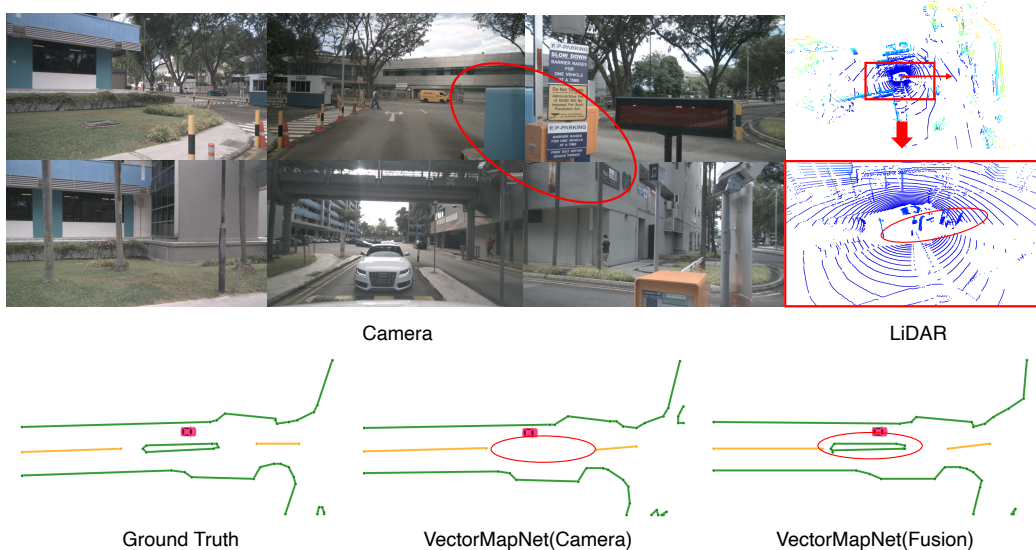


Figure 7: The blind area of onboard cameras may cause our model to miss the map elements closed ego vehicle. In contrast, we can easily find that LiDAR data has sensed some obstacles near the ego vehicle in the right-most column. With these cues, our fusion model detects the missed lane boundary by our camera-only model.

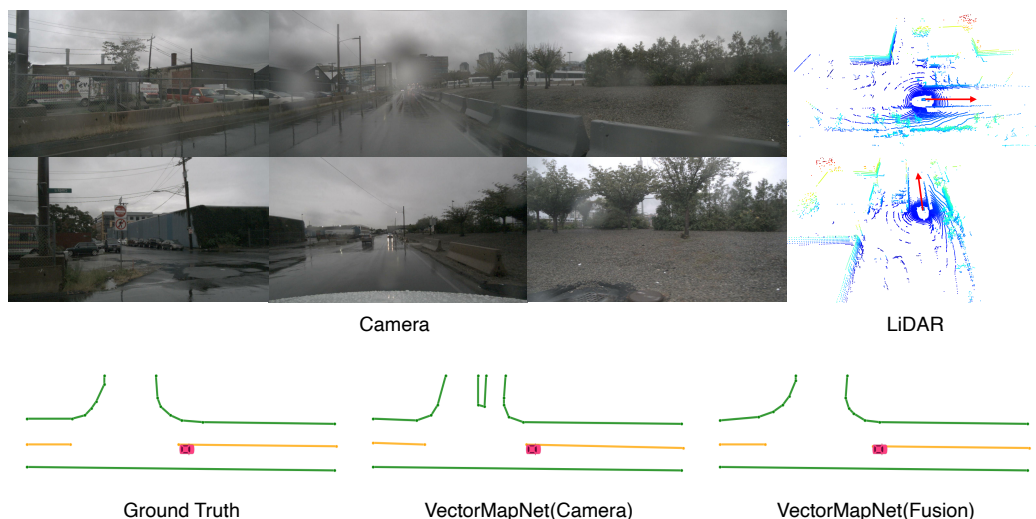


Figure 8: The qualitative results of VectorMapNet in bad weather conditions. VectorMapNet(Camera) falsely detects these puddles near the intersection as a lane boundary. The fusion result shows that the miss detection issue can be resolved by combining the depth information.

B More Visualizations of VectorMapNet (Fusion)

We visualized three cases of VectorMapNet (Fusion) and VectorMapNet (Camera) to demonstrate that LiDAR information can complement visual information to generate more robust map predictions. In the first case, the camera view is constrained by the nearby vehicles, so it can not provide helpful surrounding information. LiDAR sensor bypasses the nearby vehicle and provides some cue for VectorMapNet to generate a better result than its camera-only counterpart (see Figure 6). For the second case (see Figure 7), the model cannot detect the nearby parking gate because it locates

in the blind zone of cameras. In contrast, the LiDAR provides depth information and helps the VectorMapNet(Fusion) detect the missing lane boundary. LiDAR points can prevent the model from falsely detecting map elements in bad weather conditions as well. As shown in Figure 8, some puddles are near the intersection. With the light reflection, these puddles visually look like a lane boundary. However, the LiDAR data shows that there does not have any bump in there. Unlike the camera-only model, this depth information from LiDAR helps our fusion model not generate a non existed lane boundary.